Appendix

Appendix A:

A.1 Exploration of α-effect and turbulent diffusion

While it is generally accepted that differential rotation is the main player transforming poloidal into toroidal field the details of the processes rebuilding the poloidal field from toroidal field are still uncertain. In the mean-field language these processes are formally described as α-effect. In the near surface layers it is in principle possible to observationally constrain the amplitude of turbulent flux dispersal from models that describe the surface evolution of magnetic field.

In the context of solar dynamo models the following mechanisms for the α-effect are generally considered: 1. Helical turbulence, 2. MHD shear flow instabilities in the tachocline, 3. Rising flux tubes in the convection zone influenced by Coriolis force and convection (Babcock-Leighton). While all these processes are likely to contribute, their amplitude and spatial distribution is not known well enough to clearly quantify their individual role. Furthermore, recent research points toward a highly non-linear and also time dependent α-effect resulting from additional constraints due to conservation of magnetic helicity.

In general it is not possible to verify or rule out α-effect mechanisms within the convection zone through photospheric observations. However, some insight into the poloidal field generation mechanism might be possible. In particular measurements of the transport of magnetic flux in the polar regions by super-granular flows and meridional circulations will provide insight into efficiency of the Babcock-Leighton mechanism. Note that there is a strong correlation between the way the surface Babcock-Leighton term is modeled and quenched (in 2-D mean field models) and the resulting amplitude of the poloidal field near the poles. Precise observations of the timing, structure and strength of the poloidal field is thus key to constrain this fundamental ingredient in solar dynamo models.

A.2 Flows associated with flux emergence

An integral part of the current paradigm is the flux emergence process which consists of the buoyant rise of strong field from the base of the convection zone toward the solar surface and ultimately the formation of active regions.

Direct observations to confirm or disprove this picture are still rare but are of fundamental importance and need to be improved systematically with SOLAR-C In addition to jet like flows of a few 100 m/s that might be present at the base of the convection zone, a rising flux tube in the convective envelope induces additional motions with speeds in excess of 100 m/s based on thin-tube simulations as well as more recent 3D simulations. This flow is a superposition of the emerging upward motion and the downdraft due to the gravity and has slightly asymmetric structure in the east-west directions. A flux tube is expected to spend most of the time (about 1 month) in the lower part of the convection zone and only a few days in the upper most 20 Mm.

However, the rise speed in the near surface layers can reach values of about 1 km/s and is therefore more likely detectable.

Helioseismic signatures of sunspots have a large contribution from the near surface regions, where the relative perturbations of wave speeds are maximal. Our ability to seismically image the subsurface structure of sunspots depends strongly on a good understanding of near surface effects. The primary source of near surface thermal perturbations is caused by the Wilson depression. Independent measurements of this contribution in the near surface layers allows us to refine helioseismic tools and improve their focus on magnetic perturbations in the deeper layers. The second vantage point of a high latitude mission would allow for stereoscopic measurements of the Wilson depression, provided the imaging quality of the telescope is sufficient to resolve umbral dot like features in a sunspot umbra.

Helical turbulence generates helical mean fields. Since magnetic helicity is conserved in highly conductive fluids, small-scale magnetic helicity of the opposite sign must be shed through the photosphere or dissipated through Ohmic diffusion in order to sustain the large-scale dynamo. Evidence for helical field topologies or small-scale magnetic helicity flux through the photosphere might therefore be construed as an observational signature of the turbulent α-effect.

Vector magnetograms will also help quantify the global distribution and flux of magnetic helicity in and through the photosphere which has profound implications for the operation of the turbulent dynamo (Section3.3). High-latitude magnetograms will also enable a more thorough evaluation of the effects of surface magnetism on global oscillation frequencies, potentially improving the sensitivity of global rotational inversions. This is crucial for detecting the subtle signatures of zonal flows possibly associated with subsurface toroidal magnetic flux. In addition, observations of polar magnetism and related emission on the Sun will help interpret stellar observations by calibrating proxies used to infer magnetic activity.

Magnetic helicity is thought to play a key role on the operation of small versus large scale dynamo in the Sun. It can be demonstrated that for fast processes with respect to magnetic diffusion and by defining a reference magnetic field, a gauge invariant magnetic helicity can be defined in diffusive open system such as the Sun. It is also well known that stability conditions of the surface magnetic structures are dependent on their magnetic helicity budget and the injection of magnetic flux and helicity by the convection. This quantity can thus serve a very important role since it can relate inner and outer magnetism helping us to draw and improve our theoretical view of the solar magnetism in a more integrated way.

While it is in principle possible to detect helical flows in the convection zone or nonaxisymmetric flows resulting from MHD instabilities in the tachocline, it is not clear how to relate these flows to an α-effect without making very strong assumptions (first order smoothing, second order correlation approximation), which cannot be justified for the solar parameter range from first principles. In that sense a measurement of these flows can be taken only as an indication for a potential α-effect in these regions. On the other hand the contribution from the Babcock-Leighton α-effect can be constrained by observations of the flux-budget in the photosphere. Pure Babcock-Leighton flux-transport dynamo models typically lead to a polar (mean) field strength of about 100 Gauss (if solutions are normalized to about 10^4 Gauss at the base of the convection zone) clearly in excess of the observational constraints around 10 Gauss. The latter shows that likely additional α-effects within the convection zone or tachocline exist and it has been shown that their inclusion leads to models consistent with surface observations. A detailed study of the surface flux budget at all latitudes will promote a better understanding of the mechanisms of poloidal field regeneration in the sun. In particular, a quantitative determination of the contribution from Babcock-Leighton sources will impose additional constraints on (unobservable) sources within the convection zone and tachocline. Meanwhile, observations of magnetic helicity may be used to help assess the role of the turbulent α−effect (Section 3.3).

A.3 The inclination requirement

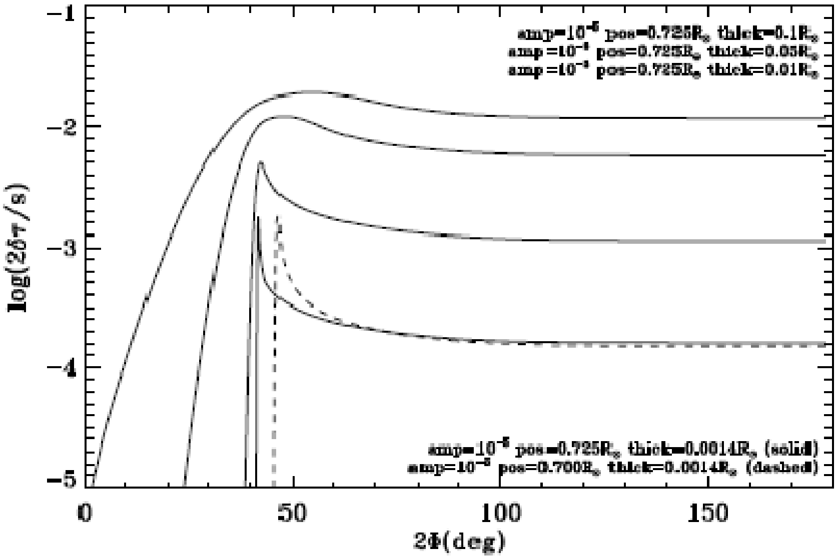

Figure 30. Travel-time perturbation 2*δτ* computed for various combination of position and thickness of soundspeed perturbation of the size 10^{-5}, against full skip angle 2*Φ*.

We have so far established that observing the sun from a high-inclination orbit may well be desirable in our attempt to study dynamical processes in the solar interior and ultimately understand the solar dynamo. The advantage we will have, however, would not be by orders of magnitude in terms of our primary observables such as, say, travel-time measurement, because projection effect is just a matter of a factor except near the very edge, where Doppler signal would be dominated by horizontal motion brought about by convection. Let us look at an example.

According to the ray theory, a ray that reaches tachocline, around r/R_{sun}~0.7 has a skip angle of ~45°. If one is aiming at observing tachocline at the solar equator and immediately beneath the disc centre, the product of two foreshortening factors, by which we lose special resolution and the vertical component of velocity, is only $\cos^2(22.5°) \sim 0.85$. It is generally believed, however, that at least some of the key dynamical features are at higher latitudes. For a ray that begins at 7.5° latitude, travels down to tachocline at 30° latitude and returns to the surface at latitude 52.5°, during all which staying within the meridian, the product is $\cos(7.5°)\cos^2(52.5°) \sim 0.6$. For a feature at higher latitudes, the figure will be worse but, it is clear that we are talking only about improvement by a factor 2 or 3. We would like to point out, however, that even a factor of 2 may turn out to be crucial at the end of the line of our investigation into the deep interior.

More complete analysis of detection capability for a certain signature in the solar interior, by time-distance helioseismology, should take the following steps.

1. Travel-time perturbation: calculate the magnitude of travel-time perturbation for a given pair of points on the solar surface for which cross-correlation function is computed. This can be done by a simple ray approximation, by a more sophisticated method such as Born approximation, or by direct numerical simulation of wave propagation.

An example-- travel-time perturbation due to sound speed anomaly near the base of the solar convection zone (Figure 30). Perturbation to travel time 2τ (here τ is the travel time from the surface to the inner turning points) has been computed for the relative sound speed perturbation $\Delta c/c = 10^{-5}$, and various position and thickness, by ray approximation. The ray path Γ is determined by local group velocity dω/dk of pure acoustic waves for which local dispersion relation ω=kc holds. Then soundspeed anomaly Δc/c is integrated over the path Γ. For flow of a similar size, measured in v/c, the integration has to be done for v cos μ/c, where μ is the angle between the path and the flow velocity. There is the reduction factor |cos μ | but if integrated over theta (see Averaging below), by rotating ray path, and if we optimize the signal, the integrated reduction factor would be just 2/π.

2. Uncertainty: calculate the uncertainty in travel time obtained for a given pair. If the pair is close to the disc centre, it is known that the so-called realization noise, caused by stochastic excitation, is the dominant source of contribution. Closer to the limb, however, and particularly if the oscillation measurement is done in Doppler, granulation noise can be important. Other quantities that are of importance to uncertainty are spatial resolution, cadence and length of observations.

The way a poor spatial resolution degrade the travel-time measurement, for example, is not through a straightly enhanced statistical uncertainties, which in fact would generally be decreased. When a group of travelling wave packets is measured with a poor resolution, there would be many components travelling between a given pair of pixels, with widely different travel time. As the dispersion in the travel time increase, the travel time between the pixels becomes increasingly ill-defined and therefore difficult to measure.

3. Averaging: Most of the time, a single measurement for just a pair of point is unlikely to yield sufficient signal-to-noise ratio. The averaging may be done in space, or in direction. To account of the effect of averaging we need to know error correlation between quantities that are (probably weighted-)summed.

A note on the direction average -- this is averaging the signal over a ray path that is rotated around the target point. Part of the averaging is about averaging product of projection factor for the pair of surface points where the individual ray begins and ends. As is seen in Figure 31, for annuli of the moderate size, it is adequate to approximate this by squaring the projection factor for the mid point (the surface point directly above the target), or a certainly point close by.

On the other hand, one can produce a fairly robust argument for the inclination requirement by limiting the objective to detection of meridional flow. The meridional flow velocity below 60° degree latitude has been measured by SOHO/MDI. From 30° latitude, therefore, one would be able to measure meridional flow up to the pole, one might think. It is true that from 30° latitude we observe a surface element at the pole as well as we would a surface element at 60° latitude from the ecliptic plane. As has already been mentioned in the above, however, there is an issue of averaging. The result obtained by Giles et al (1997) was produced by a longitudinal average within 50° from the central meridian. With the increasing latitude μ, the amount of averaging one can carry out would decrease as cos μ even if we keep the longitudinal resolution, which we will not. Let us say we would like to do at 80° latitude as well as SOHO/MDI did at the 60° latitude. By noting $(\cos(60°)/\cos(80°)^{1/2} \sim 1.7$, we can conclude that we will fall short by a factor of at least 1.7; going to 30° latitude may not be enough for measuring meridional flow close to the pole.

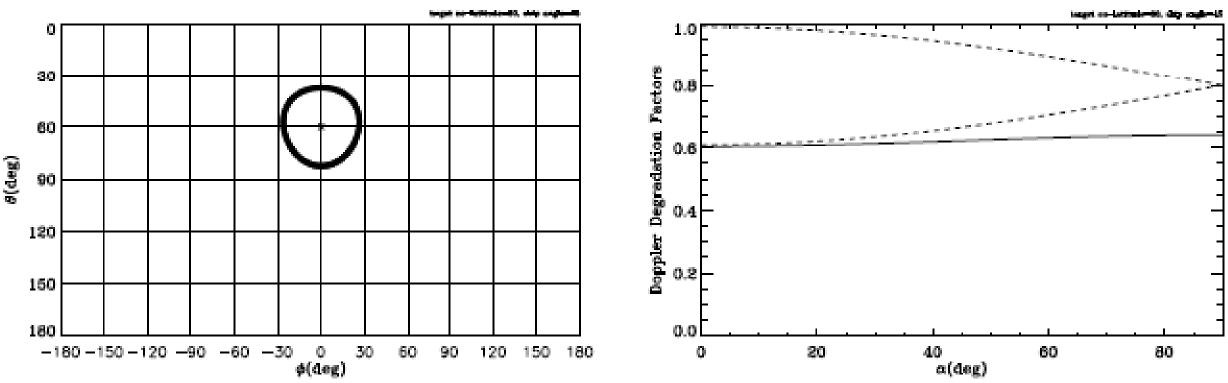

Figure 31. (left:) The path of ray-path end points when a ray with the skip angle of 45, centered around a point at 30 latitude(60 co-latitude) is rotated. (right:) The projection factors at the end points (dashed) as function of , the angle of the path to the local meridian, and its product which is nearly constant (solid)

Appendix B: Jupiter Option

Jupiter option that is described in Section 3.2 cannot reach high latitudes before the solar maximum near the early 2020's. However, the option gives an opportunity to go to high latitudes within current technology if the kick-motor for H-IIA launch vehcle is availabe. When a longer mission duration than the current Jupitor option is acceptable, there are solutions of spacecraft orbit with a higher inclination. The Jupiter option whose final orbit is similar to that of the SEP option in Sections 3.2 and 3.3 is briefly inroduced here.

B.1 Orbit Trajectory

Figure 32 shows the orbit trajectory for the Jupiter option that satisfy both the short cruise time and the maximum orbit inclination. This is essentially a balistic orbit using conventional technology. Minimum distance to the Jupiter is ~60 R_J, so that the radiation environment near the Jupiter is not severe.

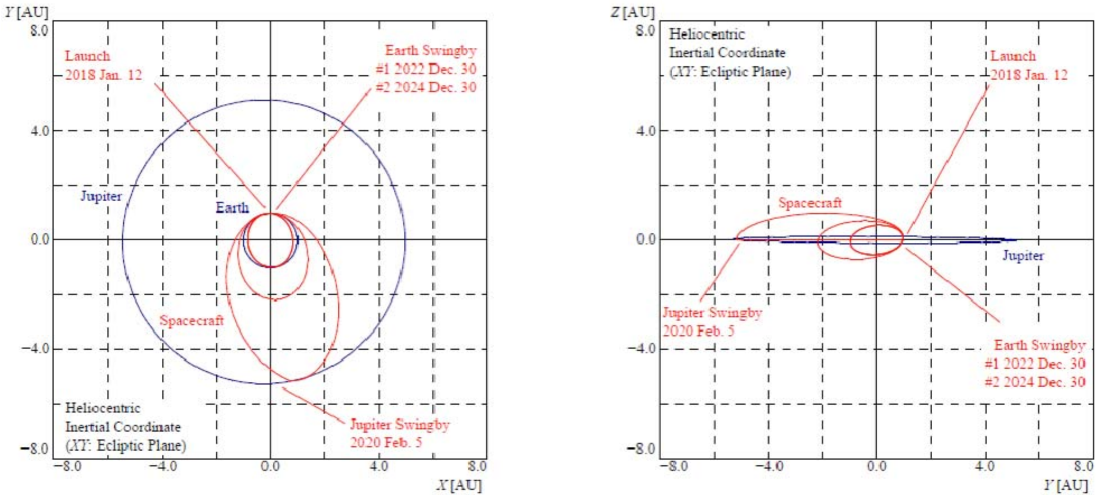

Figure 32. Trajectory profile of Jupiter option

B.2 Mission Profile

The sequence of events of Jupiter option is shown in Table 12. In this sequence, one Jupiter swingby and two Earth swingby operations form the final circular orbit of 1 AU distance from the Sun. A similar orbit is possible for the launch opportunity every ~1.1 year but the maximum orbit inclination is slitly diferent. In the case of 2019 launch, the maximum orbit inclination to the solar ecliptic plane is 36.6°

Table 12. Sequence of events of Jupiter Option

Date	Event	v_∞	i_{SEQ}
2018/01/12	Launch	8.9 km/s	7.1°
2020/02/05	Jupiter Swingby	7.3 km/s	31.4°
2022/12/30	Earth Swingby	17.0 km/s	35.6
2024/12/30	Earth Swingby	17.0 km/s	39.5°

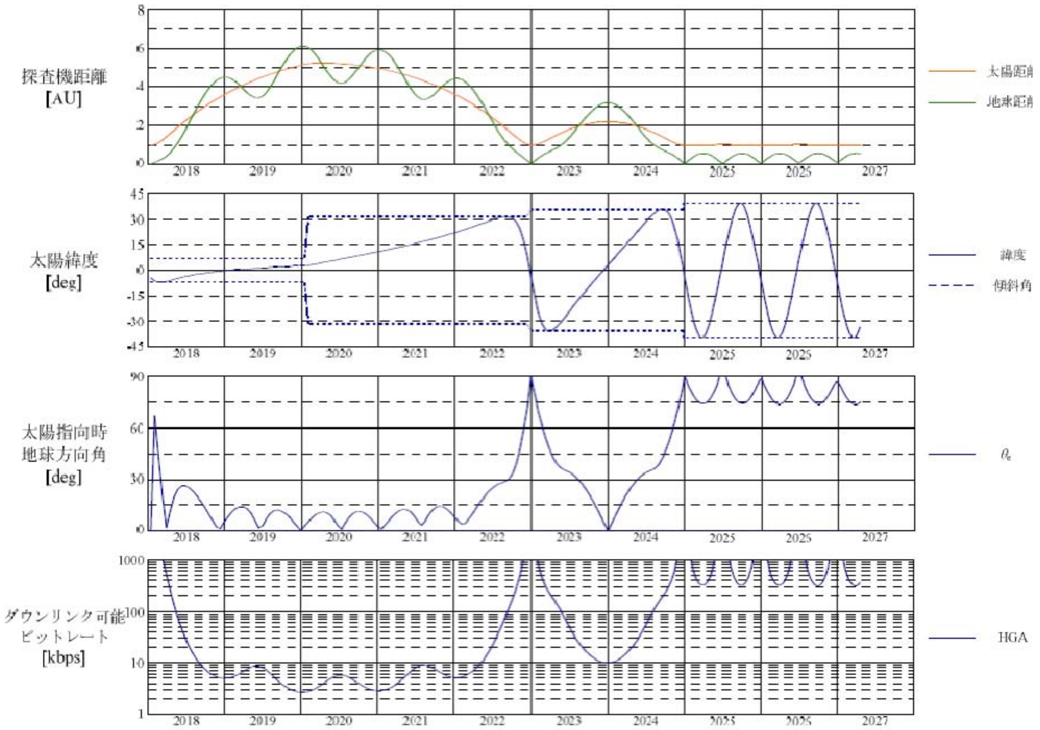

Figure 33. Mission profile of Jupiter option (to be replaced into English version)

Figure 33 shows the mission profile of Jupiter option. This indicates that the first high-data rate observations starts > 4.5 years after the launch. It takes 7 years to reach the final orbit.

B.3 Mass and Power Budget

The mass and power budget are shown in Table 13 and Table 14, respectively.

Table 13. Spacecraft mass budget of Jupiter Option

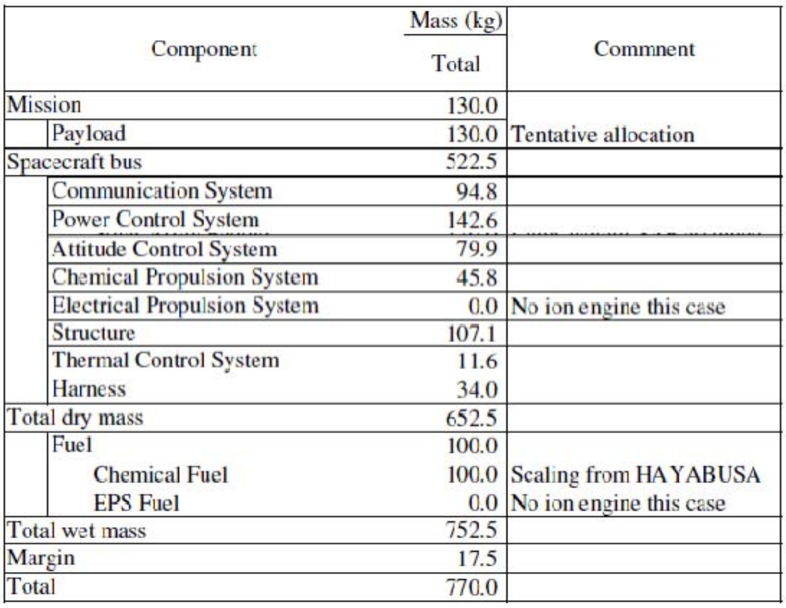

Component	Mass (kg)	Commnent
	Total	
Mission	130.0	
Payload	130.0	Tentative allocation
Spacecraft bus	522.5	
Communication System	94.8	
Power Control System	142.6	
Attitude Control System	79.9	
Chemical Propulsion System	45.8	
Electrical Propulsion System	0.0	No ion engine this case
Structure	107.1	
Thermal Control System	11.6	
Harness	34.0	
Total dry mass	652.5	
Fuel	100.0	
Chemical Fuel	100.0	Scaling from HAYABUSA
EPS Fuel	0.0	No ion engine this case
Total wet mass	752.5	
Margin	17.5	
Total	770.0	

Table 14. Spacecraft power budget of Jupiter option

Item	Power (W)	
	Near Jupiter	1 AU from Sun
Mission payload	α (TBD; heater)	150
Data hadling system	21.8	21.8
Communication system	79.0	211.3
Power supply system	37.0	51.0
Attitude control system	99.0	106.7
Chemical thruster system	250.0	4.0
Total Power	486.8+α	544.8

Appendix C: References

Belcher, J. W. & Davis, L. 1971, JGR, 76, 3534
Cirtain, J. et al. 2007, Science,
Cranmer, S. R. et al. 1999, ApJ, 511, 481
Dikpati, M. and Gilman, P. A. 2006, ApJ, 649, 498
Forbes, T. G. 2000, JGR, 105, 23153
Gabriel, A. H., 1971, Solar Phys., 21, 392
Giles, P. M., Duvall Jr, T. L., Scherrer, P. H. & Bogart, R. S. 1997, Nature, 390, 52
Haber, D. A. et al. 2002, ApJ, 570, 855
Harrison, R. A. et al. 2009, Solar Phys., 256, 219
Kamio, S. et al. 2009, A&A, 502, 345
Knaack, R. et al. 2001, A&A, 376, 1080
Kohl, J. et al. 1980, ApJ, 241, L117
Kohl, J. et al. 2006, Astron. Astrophys., Rev., 13, 31
Leighton, R. B. et al. 1962 ApJ, 135, 474
Lockwood, G. W., Skiff, B. A., Baliunas, S. L., and Radick, R. R. 1992, Nature, 360, 653
Lockwood, G. W., Skiff, B. A., and Radick, R. R. 1997, ApJ, 485, 789
McComas, D. J. et al. 2003, GRL, 30, 1517
McComas, D. J., Ebert, R. W., Elliott, H. A., Goldstein, B. E., Gosling, J. T., Schwadron, N. A., and R. M. Skoug, R. M. 2008, GRL, 35, L18103
Nakagawa, A. 2007, ApJ, 660, 1660
Parker, E. N, 1965, Planet Space Sci., 13, 949
Radick, R. R., Lockwood, G. W., Skiff, B. A., and Baliunas, S. L. 1988, ApJS, 118, 239
Raouafi, N. E. and Solanki, K. 2006, A&A, 445, 735
Reames, D. V. 1999, Space Sci. Rev., 90, 413
Richardson, I. G. and Cane, H. V. 2004, GRL, 31, L18804
Sheeley, Jr., N. R. Et al. 1997, ApJ, 484, 472
Suzuki, T., and Inutuka, S. 2005, ApJ, 632, L49
Thomas, R. 2003, SPIE, 4853, 417
Thompson, M. J. et al. 1996, Sci, 272, 1300
Tsuneta, S., et al. 2008, ApJ, 688, 1374
Vorontsov, S. V. 2002, Sci, 296, 101
Waldmeier, M., Die Sonnenkorona, Vol. 2, Verlag Birkhäuser 1957.

Appendix D: Acronyms

ACE	Advanced Composition Exploler (spacecraft)
ACS	Attitude Control System
AR	Active Region
ARD	Aerospace Research and development Directorate
BAT	Battery
CCD	Charge Coupled Device
CFRP	Carbon Fiber Reinforced Plastic
CH	Coronal Hole
CIR	Co-rotation Interaction Region
CME	Coronal Mass Ejection
CMOS	Complementary Metal Oxide Semiconductor
CZ	Convection Zone
DHU	Data Handling Unit
DIM	Direct Inclining Method
DPCM	Differential Pulse Code Modulation (,a type of digital communications method)
DSN	Deep Space Network
EAI	EUV Activity Imager proposed for SOLAR-C Plan-A
EDVEGA	Electric Propulsion Delta-V Earth Gravity Assist
EGA	Earth Gravity Assist
EIS	EUV Imaging Spectrometer (on Hinode spacecraft)
EM	Engineering Model
ESA	European Space Agency
ESS	EUV Scanning Spectrometer proposed for SOLAR-C Plan-A
EUV	Extreme UltraViolet
EUVI	EUV Imager (on STEREO spececrafts)
FOV	Field Of View
FWHM	Full Width at Half Maximum
GCR	Galactic Cosmic Rays
GONG	Global Oscillation Network Group (by observing the Sun with six ground-based observatories for helioseismology)
HAI	Helioseismic Activity Imagier proposed for SOLAR-C Plan-A
HCE	HouseKeeing Electronics
HK	HouseKeeping
HMI	Helioseismic Magnetic Imager (on Solar Dynamics Observatory)
HS	HelioSeismology
ICME	Interplanetary Coronal Mass Ejection a type of digital communications method
IEM	Ion Engine Module
IES	Ion Engine System
IHI	Inner Heliospheric Imager proposed for SOLAR-C Plan-A
IPM	IES Pointing Mechanism
IPS	InterPlanetary Scintillation
IPU	IES Power Unit
ISAS	Institute of Space and Astronautical Science
ISP	SPecific Impulse
ITA	Ion Thruster Assembly

ITCU	Ion Thruster Control Unit
JAXA	Japanese Aerospace Exploration Agency
JGA	Jupiter Gravity Assist
JPEG	Joint Photographic Experts Group (, a group which created a data compression)
JPL	Jet Propulsion Laboratory
LASP	Laboratory for Atmospheric and Space Physics
LIM	Luminosity and Irradiance Monitor proposed for SOLAR-C Plan-A
MDI	Michelson Doppler Imager (on SOHO)
MHD	Magneto-HydroDynamics
MLI	Multi-Layer Insulator
MMO	Mercury Magnetospheric Orbiter
MSU	Microwave Supply Unit
NAOJ	National Astronomical Observatory of Japan
NASA	National Aereopace Agency
PCU	Power Control Unit
PMOD	Physikalisch-Meteorologisches Observatorium Davos
PMU	Propellant Management Unit
PREMOS	PREcision MOnitor Sensor on PICARD spacecraft for monitring TSI
PYC	Pyrotechnic Controller
QS	Quiet Sun
RW	Reaction Wheel
RZ	Radiative Zone
SAP	Solar Array Panel
SDO	Soalr Dynamics Observatory (spacecraft)
SEM	Sequential EDVEGA Method
SEP	Solar Energetic Particle in science part or Solar Electric Propulsion in engineering
SOHO	Solar and Heliospheric Observatory (spacecraft)
SORCE	SOlar Radiation and Climate Experiment (spacecraft)
SOT	Solar Optical Telescope on Hinode spacecraft
SSR	Serieis Switching Regulator
STEREO	Solar TErrestrial RElations Observatory (spacecrafts)
TCIM	Telemetry Command Interface Module
TIM	Total Irradiance Monitor (on SORCE)
TR	Transition Region
TRL	Technical Readiness Level
TSI	Total Solar Irradiance (on SORCE spacecraft)
UV	UltraViolet
UVCS	UltraViolet Coronagraph Spectrometer (on SOHO)
VGA	Venus Gravity Assist
VIRGO	Variability of solar IRradiance and Gravity Oscillations (on SOHO)
XRT	X-Ray Telescope (on Hinode spacecraft)